

On the Origin of Flux Ratio Anomaly in Quadruple Lens Systems

Kaiki Taro Inoue^{1*}

¹*Faculty of Science and Engineering, Kindai University, Higashi-Osaka, 577-8502, Japan*

9 December 2024

ABSTRACT

We explore the origin of flux ratio anomaly in quadruple lens systems. Using a semi-analytic method based on N -body simulations, we estimate the effect of possible magnification perturbation caused by subhaloes with a mass scale of $\lesssim 10^9 h^{-1} M_{\odot}$ in lensing galaxy haloes. Taking into account astrometric shifts by perturbers, we find that the expected change to the flux ratios per a multiply lensed image is just a few percent and the mean of the expected convergence perturbation at the effective Einstein radius of the lensing galaxy halo is $\langle \delta\kappa_{\text{sub}} \rangle = 0.003$, corresponding to the mean of the ratio of a projected dark matter mass fraction in subhaloes at the effective Einstein radius $\langle f_{\text{sub}} \rangle = 0.006$. In contrast, the expected change to the flux ratio caused by line-of-sight structures with a mass scale of $\lesssim 10^9 h^{-1} M_{\odot}$ in intergalactic spaces is typically ~ 10 percent and the mean of the convergence perturbation is $\langle |\delta\kappa_{\text{los}}| \rangle = 0.008$, corresponding to $\langle f_{\text{los}} \rangle = 0.017$. The contribution of magnification perturbation caused by subhaloes is ~ 40 percent of the total at a source redshift $z_S = 0.7$ and decreases monotonically in z_S to ~ 20 percent at $z_S = 3.6$. Thus it is likely that the dominant contribution comes from line-of-sight structures. Assuming statistical isotropy, the convergence perturbation estimated from observed 11 quadruple lens systems has a positive correlation with the source redshift z_S , which is much stronger than that with the lens redshift z_L . This feature also supports the idea that the flux ratio anomaly is caused mainly by line-of-sight structures rather than subhaloes. We also discuss about a possible imprint of line-of-sight structures in demagnification of minimum images due to locally underdense structures in the line of sight. The possibility of finding such an “anomalous anomaly” is expected to be 30-40 percent for a minimum image that shows an anomaly in the relative flux.

Key words: galaxies: formation - cosmology: theory - gravitational lensing - dark matter.

1 INTRODUCTION

It has been known that some quadruply lensed quasars show anomalies in the observed flux ratios of lensed images provided that the gravitational potential of the lensing galaxy halo is sufficiently smooth. Such a discrepancy is called the “anomalous flux ratio” and has been considered as an imprint of cold dark matter (CDM) subhaloes with a mass of $\sim 10^{8-9} M_{\odot}$ in the parent galaxy haloes (Mao & Schneider 1998; Metcalf & Madau 2001; Chiba 2002; Dalal & Kochanek 2002; Keeton et al. 2003; Inoue & Chiba 2003; Kochanek & Dalal 2004; Metcalf et al. 2004; Chiba et al. 2005; Sugai et al. 2007; McKean et al. 2007; More et al. 2009; Minezaki et al. 2009; Xu et al.

2009, 2010; Vegetti et al. 2012; Fadely & Keeton 2012; MacLeod et al. 2013; Vegetti et al. 2014).

However, intergalactic halos in the line of sight can act as perturbers as well (Chen et al. 2003; Metcalf 2005; Xu et al. 2012). Indeed, taking into account of astrometric shift, recent studies have found that the observed anomalous flux ratios can be explained solely by line-of-sight structures with a surface density $\sim 10^{7-8} h^{-1} M_{\odot}/\text{arcsec}^2$ (Inoue & Takahashi 2012; Takahashi & Inoue 2014; Inoue et al. 2015b,a) without taking into account subhaloes in the lensing galaxies. Moreover, using the cusp and fold caustic relations expressed in statistics R_{cusp} and R_{fold} , Xu et al. (2015) found that the perturbation caused by subhaloes is not sufficient for explaining the observed anomalies.

In order to model the lens systems, in some lenses, one must take into account other massive objects that

* E-mail: kinoue@phys.kindai.ac.jp

may significantly affect the flux ratios (McKean et al. 2007; More et al. 2009). Moreover, disk components can also significantly perturb the flux ratios (Hsueh et al. 2016). Thus, it is sometimes difficult to make constraints using the cusp and fold caustic relations because they hold only in lenses with a smooth potential and small angles between two bright lensed images.

In this paper, we investigate the origin of flux ratio anomaly in 11 quadruple lens systems including radio and mid-infrared (MIR) fluxes. We do not use the “traditional” statistics R_{cusp} and R_{fold} in literature. The reasons are: 1) the lens systems can have a more complex structures such as a secondary and a third lens. 2) the cusp and fold caustic relations do not exactly hold because the angle between two images in a triplet or a double is not necessarily small. 3) the magnification bias in the selection of lens candidates can significantly affect the statistics. We also use the information of possible astrometric shifts, which was often ignored in literature (see, however, Chen et al. (2007); Sluse et al. (2012)). Furthermore, we pay attention to the correlation between the perturbation to the fluxes and the redshifts of the primary lenses and the source, which would shed a new light on the origin of the flux ratio anomaly.

In section 2, we estimate the perturbation effect caused by subhaloes in lensing galaxies using a semi-analytic mass function of subhaloes. In section 3, we briefly describe our method for calculating the perturbation effect caused by line-of-sight structures. In section 4, we briefly describe the 11 quadruple lenses. In section 5, we explain the lens model of an unperturbed system. In section 6, we explain our method using a statistic “ η ” for fitting the model to the data. In section 7, we show our result for the magnification and convergence perturbations and their correlations with the lens and source redshifts. In section 8, we briefly discuss about a new type of anomaly that can be used for distinguishing the origin of perturbation.

In what follows, we assume a cosmology with a matter density $\Omega_{m,0} = 0.3134$, a baryon density $\Omega_{b,0} = 0.0487$, a cosmological constant $\Omega_{\Lambda,0} = 0.6866$, a Hubble constant $H_0 = 67.3$ km/s/Mpc, a spectral index $n_s = 0.9603$, and the root-mean-square (rms) amplitude of matter fluctuations at $8h^{-1}$ Mpc, $\sigma_8 = 0.8421$, which are obtained from the observed CMB (Planck+WMAP polarization; Planck Collaboration et al. (2014)).

2 SUBSTRUCTURE LENSING

In order to estimate the magnification perturbation due to subhaloes in a lensing galaxy halo, we need to calculate the mass function of subhaloes.

At a proper distance R from the centre of a parent halo, the number density of subhaloes n per a logarithmic interval of the mass m_{in} of subhaloes at the infall is well approximated by

$$\frac{dn(m_{\text{in}}, R)}{d \ln m_{\text{in}}} \propto m_{\text{in}}^{-\alpha} \rho(R), \quad (1)$$

where $\rho(R)$ is the density of the parent halo at R and $\alpha \sim 0.9^1$.

¹ In literature, the other definition $\tilde{\alpha} = \alpha + 1$ is sometimes used

However, after infalling, the mass of subhaloes are stripped off by the tidal force of the parent halo, and some of them are completely disrupted. Therefore, the mass m of subhaloes at the time of deflection of photons can be significantly reduced at the position of lensed images.

Assuming that subhaloes have a density profile similar to that of an singular isothermal sphere (SIS), the bound fraction $\mu = m/m_{\text{in}}$ of subhaloes at R can be approximated as

$$\mu(R) \propto R^\beta, \quad (2)$$

where $\beta \sim 1$ if the kinetic energy of subhaloes is negligible. In real setting, one must also consider the kinetic energy of a subhalo at the time of infall and the change of tidal stripping that depends both on the orbit and the background gravitational field. If the tidal stripping of each subhalo can be treated as an uncorrelated random process, one may approximate the set of bound fraction μ for each subhalo as random variables. Assuming that μ is written in terms of a polynomial and obeys a log-normal distribution and the the spatial distribution with a given infall mass traces the mass density profile, based on two sets of high-resolution cosmological N -body simulations, the Aquarius (Springel et al. 2008) and Phoenix (Gao et al. 2012) simulation suites, Han et al. (2015) obtained a subhalo mass function for a parent halo with R_{200} and M_{200} ,

$$\frac{dn(m, R)}{d \ln m} = A_{\text{acc}} B f_s e^{\sigma^2 \alpha^2 / 2} \left[\frac{m}{m_0 \bar{\mu}(R)} \right]^{-\alpha} \frac{\rho(R)}{m_0}, \quad (3)$$

where the mean bound fraction is

$$\bar{\mu}(R) = \mu_* \left(\frac{R}{R_{200}} \right)^\beta \quad (4)$$

and

$$\begin{aligned} \mu_* &= 0.5 (M_{200}/m_0)^{-0.03}, \quad \alpha = 0.95, \\ \beta &= 1.7 (M_{200}/m_0)^{-0.04}, \quad A_{\text{acc}} = 0.1 (M_{200}/m_0)^{-0.02} \\ f_s &= 0.55, \quad m_0 = 10^{10} h^{-1} M_\odot. \end{aligned} \quad (5)$$

Let us assume that a parent halo that hosts a primary lensing galaxy has an NFW profile with a concentration parameter C and a critical density ρ_{crit} at a redshift z ,

$$\rho^{NFW}(R) = \frac{\delta_c(C) \rho_{\text{crit}}(z)}{(R/R_{-2})(1 + R/R_{-2})^2}, \quad (6)$$

where

$$R_{-2} = R_{200}/C, \quad \delta_c(C) = \frac{200}{3} \frac{C^3}{\ln[1 + C] - C/(1 + C)}. \quad (7)$$

Integrating equation (3) over the line of sight, we obtain the mass function projected onto the lens plane as a function of m and the projected proper distance R_{2D} to the parent halo center in the lens plane as

$$\begin{aligned} \frac{dn_s(m, R_{2D})}{d \ln m} &= A_{\text{acc}} B f_s e^{\sigma^2 \alpha^2 / 2} \left[\frac{m}{m_0} \right]^{-\alpha} \frac{\delta_c(C) \rho_{\text{crit}}(z)}{m_0} \\ &\times K[R_{2D}, R_{200}/C, \gamma], \end{aligned} \quad (8)$$

where n_s is the surface number density, $\gamma = \alpha\beta$ and

$$\begin{aligned}
 & K[R_{2D}, R_{200}/C, \gamma] \\
 &= 2^{2-\gamma} \mu_*^\alpha \frac{R_{200}^{-\gamma} R_{2D}^{-3+\gamma} R_{-2}^3}{\Gamma[3-\alpha\beta](R_{2D}^2 - R_{-2}^2)} \\
 &\times \left[(\Gamma[3/2 - \gamma/2])^2 R_{-2} \left((-2 + \gamma) R_{2D}^2 - (R_{-2}^2 + \gamma(R_{2D}^2 \right. \right. \\
 &\left. \left. - R_{-2}^2) \right) {}_2F_1 \left[1, \frac{3-\gamma}{2}, 2 - \frac{\gamma}{2}, \frac{R_{-2}^2}{R_{2D}^2} \right] \right) \\
 &+ \Gamma[1 - \gamma/2] \Gamma[2 - \gamma/2] R_{2D} (R_{2D}^2 - R_{-2}^2) \\
 &\times {}_3F_2 \left[1, \frac{3}{2}, \frac{1-\gamma}{2}; \frac{1}{2}, \frac{3-\gamma}{2}; \frac{R_{-2}^2}{R_{2D}^2} \right] \right]. \quad (9)
 \end{aligned}$$

Equations (8) and (9) give the surface mass density Σ_s and the surface number density n_s of subhaloes at a distance R_{2D} in an NFW halo,

$$\Sigma_s(R_{2D}) = \int_{m_{min}}^{m_{max}} \frac{dn_s(m, R_{2D})}{d \ln m} dm, \quad (10)$$

$$n_s(R_{2D}) = \int_{m_{min}}^{m_{max}} \frac{dn_s(m, R_{2D})}{d \ln m} d \ln m, \quad (11)$$

where m_{min} and m_{max} are the minimum and the maximum mass of the subhaloes. Note that the obtained sub-

halo surface number densities are consistent with those in (Xu et al. 2015) in which 500 random projections are used per halo in the Aquarius and Phoenix simulations. As we shall show in section 7, the effective Einstein radius is $R_E \sim 0.01 R_{200}$. As shown in Fig. 1, at projected proper distances $R_{2D} \lesssim 0.03 R_{200}$, for $M_{200} = 10^{12-13} h^{-1} M_\odot$, the surface mass density is nearly constant due to tidal disruption. Since for $R_{2D} < R_{-2}$, the most of the surface mass density of an NFW (or SIS) halo is determined by masses whose mass density has a slope of ~ -2 , the contribution of masses at inner regions whose mass density has a slope of ~ -1 is small. Then the surface mass density can be approximately written as

$$\Sigma_s(R_{2D}, m) \sim m^{-\alpha} R_{2D}^{\alpha\beta} R_{2D}^{-1}. \quad (12)$$

Assuming that $\alpha \sim \beta \sim 1$ for NFW haloes, equation (12) gives $\Sigma_s(R_{2D}, m) \approx m^{-\alpha}$. Thus Σ_s does not depend on R_{2D} . Setting $R_{2D} = 0$, we can obtain an approximated formula for the surface mass density at $R_{2D} \lesssim R_E$,

$$\begin{aligned}
 \Sigma_s(R_E) &\approx \frac{\mu_*^\alpha m_0^{\alpha-1}}{1-\alpha} \left[m_{max}^{1-\alpha} - m_{min}^{1-\alpha} \right] \\
 &\times e^{\sigma^2 \alpha^2 / 2} J[\gamma, R_{200}, C; z], \quad (13)
 \end{aligned}$$

and

$$\begin{aligned}
 n_s(R_E) &\approx \frac{\mu_*^\alpha m_0^{\alpha-1}}{\alpha} \left[-m_{max}^{-\alpha} + m_{min}^{-\alpha} \right] \\
 &\times e^{\sigma^2 \alpha^2 / 2} J[\gamma, R_{200}, C; z], \quad (14)
 \end{aligned}$$

where

$$\begin{aligned}
 J[\gamma, R_{200}, C, z] &\equiv 2\pi A_{acc} B f_s (1-\gamma) \csc(\gamma\pi) R_{200} \\
 &\times C^{-(1+\gamma)} \delta_c(C) \rho_{crit}(z). \quad (15)
 \end{aligned}$$

Here a condition $0 < \gamma < 2$ should be satisfied in order to avoid divergence.

The surface mass density of an NFW lensing galaxy halo is given by

$$\begin{aligned}
 \Sigma_0(R_{2D}) &= \left[\frac{2R_{-2}^3}{R_{2D}^2 - R_{-2}^2} + \frac{4R_{-2}^4}{(R_{-2}^2 - R_{2D}^2)^{3/2}} \right] \\
 &\times \operatorname{arccoth} \left[\frac{R_{2D} + R_{-2}}{(R_{-2}^2 - R_{2D}^2)^{1/2}} \right] \delta_c(C) \rho_{crit}(z). \quad (16)
 \end{aligned}$$

Then, the ratio of the convergence of subhaloes κ_s to that of the parent NFW halo κ_0 can be obtained from equations (3)-(11) and (16). As shown in Fig. 2, the ratio increases in R_{2D} . At $R_{2D}/R_{200} \sim 0.01$, the dependence on R_{2D} is determined solely by the surface mass density of an NFW parent halo as κ_s is nearly constant. The slope is slightly flatter than R_{2D}^{-1} , because the effective Einstein radius is smaller than the scale radius $R_{2D}/R_{200} \sim 0.01 < R_{-2}/R_{200} \sim 0.1$. As we shall show later, the ratio κ_s/κ_0 gives an upper limit for the dark matter fraction f at the position of lensed images, which characterizes the strength of contribution from subhaloes.

3 LINE-OF-SIGHT LENSING

To take into account the non-linear effects of line-of-sight structures, we first calculate the non-linear power spectra of matter fluctuations down to mass scales of $\sim 10^5 h^{-1} M_\odot$ using N -body simulations Inoue & Takahashi (2012); Takahashi & Inoue (2014). For simplicity, we do not consider baryonic effects in our simulations. In the following, we assume that perturbations of flux of images due to shifts of positions are sufficiently smaller than those due to distortion of the images. Then the magnification contrast $\delta^{\tilde{\mu}} = \delta\tilde{\mu}/\tilde{\mu}$ of each lensed image for a background lens model with a convergence κ and a shear γ can be approximated as

$$\delta^{\tilde{\mu}} \approx \frac{2(1-\kappa)\delta\kappa + 2\gamma\delta\gamma}{(1-\kappa)^2 - \gamma^2}, \quad (17)$$

where $\delta\kappa$ and $\delta\gamma$ are the convergence and shear due to perturbers in the line of sight. Using equation (17), we can estimate the magnification contrast for each lens using the semi-analytic formulae developed in Inoue & Takahashi (2012); Takahashi & Inoue (2014). We also take into account the astrometric shifts due to line-of-sight structures, which are often overlooked in the literature. For details, see also Inoue et al. (2015b).

4 QUADRUPLE LENS SYSTEMS

In this paper, we use 10 QSO-galaxy quadruple lens systems, namely, B1422+231, B0128+437, MG0414+0534, B1608+656, B0712+472, B2045+265, H1413+117, PG1115+080, Q2237+0305, RXJ1131-1231 and an SMG-galaxy system SDP.81. We exclude the spiral lens B1933+503, because it has a very complex structure. Similarly, we also exclude B1555+375 that has a disc component (Hsueh et al. 2016). However, we include Q2237+0305 as the buldge component of the spiral lensing galaxy dominates over the disk component. In our analysis, we use observed MIR fluxes for MG0414+0534, H1413+117, PG1115+080, Q2237+0305 and RXJ1131-1231 and radio

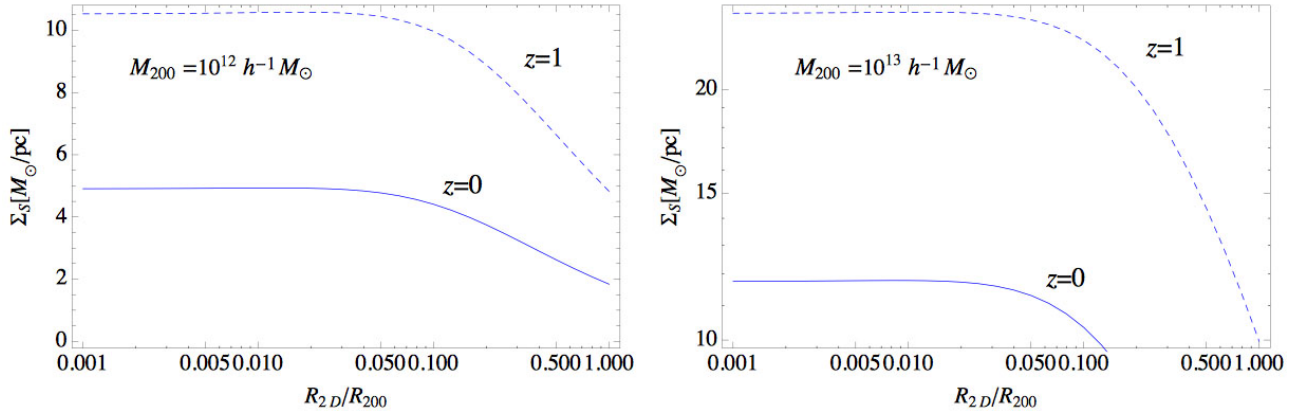


Figure 1. Surface mass density of subhaloes at a normalised distance R_{2D}/R_{200} for $M_{200} = 10^{12} h^{-1} M_{\odot}$ (left) and $M_{200} = 10^{13} h^{-1} M_{\odot}$ (right).

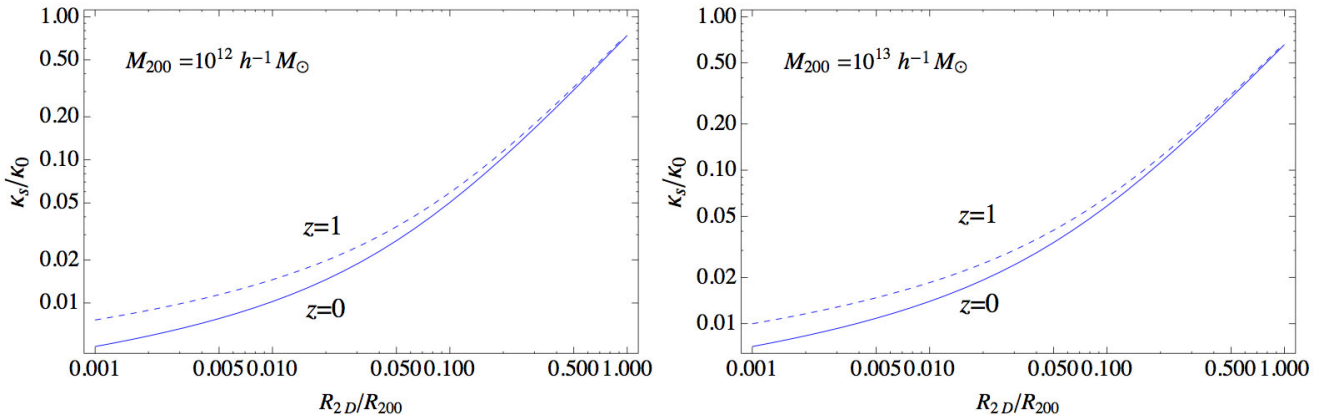


Figure 2. Ratio of the convergence of subhaloes to that of the parent NFW halo at a normalised distance R_{2D}/R_{200} for $M_{200} = 10^{12} h^{-1} M_{\odot}$ (left) and $M_{200} = 10^{13} h^{-1} M_{\odot}$ (right).

fluxes averaged over a certain period for B1422+231, B0128+437, B1608+656, B0712+472 and B2045+265. For the astrometry of lensed images and the centroids of lensing galaxies, we use optical or NIR data except for the SDP.81 in order to avoid bias due to complex structures of jets. We also use time delay for modeling B1608+656. For the SDP.81, we use the processed archival image of the band 7 continuum taken from the ALMA Science Portal (see [ALMA Partnership et al. \(2015\)](#) for detail) and for the flux ratios of lensed images, we use fluxes in an aperture radius 0.04 arcsec defined in the source plane. For detail of these 11 lens systems, see [Takahashi & Inoue \(2014\)](#); [Inoue et al. \(2015b,a\)](#).

In table 1, we show the redshifts of the source z_S and those of the primary lens z_L , the observed wavelength band of position and flux of lensed images, the number of lensed images N used for constraining the lens model. The radius R_S of a MIR continuum source is estimated using dust reverberation, and R_S of a radio source is estimated from the apparent angular sizes (typically $1 \sim 3$ mas in radius) of lensed very long baseline interferometry images. For the SDP.81, we adopt the beam size in the ALMA band 7 continuum image as the source size, though it may have a smaller structure. The wavenumber is defined as $k_S \equiv 2\pi/(4r_S)$, where r_S is

the comoving radius of a source. k_S is used as the upper limit of wavenumber in estimating η from line-of-sight structures.

5 LENS MODEL

As a fiducial model of primary lensing galaxy haloes, we adopt a singular isothermal ellipsoid (SIE) ([Kormann et al. 1994](#)), which can explain flat rotation curves. There is considerable evidence in favor of the isothermal profile, and the properties of gravitational potential near the Einstein radius are insensitive to the radial mass distribution ([Koopmans et al. 2009](#); [Humphrey & Buote 2010](#); [Barnabè et al. 2011](#); [Oguri et al. 2014](#)). We use the fluxes of lensed images, the relative positions of lensed quadruple images and the centroid of lensing galaxies and time delay of lensed images if available. The contribution from groups, clusters, and large-scale structures at angular scales larger than the Einstein radius of the primary lens is taken into account as an external shear (ES). The parameters of the SIE('s) plus ES model are the effective Einstein radius b (defined in [Kormann et al. \(1994\)](#)), the apparent ellipticity e of the lens and its position angle θ_e , the strength and the direction of the external shear (γ, θ_γ), the lens position

(x_G, y_G) , the source position (x_s, y_s) . The Hubble constant h is also treated as a model parameter. The angles θ_e and θ_γ are measured in East of North expressed in the observer's coordinates (see Table 4). We modeled the secondary lenses in MG0414+0534, H1413+117, B1608+656 and B2045+265 by either an SIS or SIE.

To find a set of best-fit parameters, we use a numerical code GRAVLENS² developed by Keeton in order to implement the simultaneous χ^2 fitting of the fluxes, positions, and time delay of lensed images (if reliable data is available) and the positions of centroid of lensing galaxies. The best-fitted model parameters are in Inoue & Takahashi (2012); Takahashi & Inoue (2014).

6 METHOD

In order to measure the magnification perturbation of lensed images, we use a statistic η defined as

$$\eta \equiv \left[\frac{1}{2N_{\text{pair}}} \sum_{i \neq j} \left[\delta_i^{\tilde{\mu}}(\text{minimum}) - \delta_j^{\tilde{\mu}}(\text{saddle}) \right]^2 \right]^{1/2}, \quad (18)$$

where $\delta_i^{\tilde{\mu}}(\text{minimum})$ and $\delta_j^{\tilde{\mu}}(\text{saddle})$ are magnification contrasts corresponding to the minimum and saddle images and N_{pair} denotes the number of pairs of lensed images. If the correlation of magnification between pairs of images is negligible, then η corresponds to the mean magnification perturbation per a lensed image. Perturbation by locally overdense structures would boost η as the saddle images tend to be demagnified whereas the minimum images are always magnified if the astrometric shift of lensed images is negligible. Note that we need to fix the primary lens model (i.e., a best-fitted model without line-of-sight structures or subhaloes) in order to calculate η . In other words, η is a model dependent statistic though it can be calculated from the observed flux ratios.

The mean and the standard deviation of η can be calculated as follows. First, we estimate the perturbation ε of the largest angular separation θ_{max} between a pair of lensed images X and Y,

$$\varepsilon = |\delta\theta(X) - \delta\theta(Y)|, \quad (19)$$

where $\delta\theta$ represents the astrometric shift perturbation of a lensed image at θ in the lens plane. We then assume that the perturbation satisfies $\varepsilon \leq \varepsilon_0$ where ε_0 is the observational error for the largest angular separation. This condition gives an approximated upper limit on the contribution of line-of-sight structures or subhaloes assuming that the gravitational potential of the primary lens is similar to that of an SIS and sufficiently smooth on the scale of the effective Einstein radius (see appendix). Note, however, that if the astrometric shift caused by a possible local perturber is parallel to the tangential arc of a lensed image, though the possibility is small for a point source, the condition is too strict to some extent³.

² See <http://redfive.rutgers.edu/~keeton/gravlens/>

³ For an extended source, some systems show an Einstein ring in which the magnification is significantly large. In this case, perturbers in the line of sight to the ring (if present) can cause degeneracy with macromodel.

In the cases of line-of-sight lensing, we also assume that small-scale modes with a wavelength larger than the mean comoving separation $\langle b \rangle$ between the lens center and lensed images at the primary lens plane are significantly suppressed. Any modes whose fluctuation scales are larger than $\langle b \rangle$, which is roughly the size of the comoving effective Einstein radius, contribute to the smooth component of a primary lens, namely, a constant convergence and shear. Therefore, we consider only modes whose wavenumbers satisfy $k > k_{\text{lens}}$ where $k_{\text{lens}} \equiv \pi/(2\langle b \rangle)$. Even if the cutoff is applied, sometimes the condition $\varepsilon \leq \varepsilon_0$ cannot be satisfied due to a presence of a possible secondary lens or other lenses. In this case, we further cutoff the small-scale fluctuations with a wavenumber $k > k_{\text{lens}}$ using the so-called ‘‘constant-shift (CS) cut’’ (Takahashi & Inoue 2014). Roughly speaking, the CS cut leads to a uniform suppression of astrometric shift perturbation with wavenumbers of $k_{\text{lens}} < k < k_{\text{cut}}$. Using the non-linear power spectrum with the CS cut, we can estimate the second moment of $\langle \eta^2 \rangle$. From the fitted function of η in (Takahashi & Inoue 2014), we can obtain a simple formula $\langle \eta \rangle \sim 0.85 \langle \eta^2 \rangle^{1/2}$ and the standard deviation $\delta\eta = 0.53 \langle \eta^2 \rangle^{1/2}$, which agrees with the fitted function within a percent level for $\langle \eta^2 \rangle^{1/2} < 0.2$.

In the cases of substructure lensing, we assume that subhaloes whose maximum astrometric shift (at $R = R_{-2}$ for an NFW halo) exceeds ε_0 at the time of infall do not perturb the lens system, which determine the maximum mass of subhaloes m_{200}^{max} . This assumption is a reasonable one as long as the relevant subhaloes have a mass profile similar to an SIS. Although the tidal heating causes a concentration of subhalo mass near the center, most of light rays pass through the outer region of subhaloes where the effect of tidal heating is much small. Therefore, we expect that the change of inner mass profile is not relevant to the astrometric perturbation. We also neglect masses below m_{200}^{min} for which the perturbation to the magnification caused by a corresponding SIS (having the same astrometric shift at $R = R_{-2}$) centred at a source is less than ~ 0.1 percent due to the finite source size R_S .

In order to estimate the mass profile of subhaloes at the time of infall, we use a semi-analytic model of NFW haloes (only dynamically relaxed ones) in which the concentration parameter $C = C(M_{200}, z_{\text{infall}})$ is given by

$$\log_{10} C = \alpha + \beta \log_{10}(M_{200}/M_\odot) [1 + \gamma (\log_{10}(M_{200}/M_\odot))^2], \quad (20)$$

where α, β, γ are constant parameters and $z_{\text{infall}} \leq 4$ (Correa et al. 2015).

As for the infall redshift, we assume that $0 < z_{\text{infall}} < 4$ and the mean is given by $\langle z_{\text{infall}} \rangle \sim 2$ (Emberson et al. 2015). Since the infall redshift z_{infall} of massive subhaloes tends to be smaller than this value, we take the ambiguity of $\Delta z_{\text{infall}} = 2$ into account in estimating the mean of the convergence perturbation $\delta\kappa$ due to subhaloes.

For estimating the shear perturbation $\delta\gamma$, we assume statistical isotropy for the perturbation. Then we have $|\delta\gamma| \sim |\delta\kappa|$ and we can estimate the magnification contrast $\delta\mu$ and $\langle \eta \rangle$ for subhaloes. In a similar manner, assuming statistical isotropy, we can estimate the strength of the convergence perturbation $|\delta\kappa|$ from observed η . Note that the relation is exact for SISs. Furthermore, we neglect a possible spatial correlation between perturbers at different positions

of lensed images. In the case of line-of-sight structures, we find that the correlation effect is ~ 10 percent for lenses with a fold caustic and much smaller for those with a cusp caustic. Thus, this approximation yields at most ~ 10 percent errors in $|\delta\kappa|$ estimated from η . In the case of subhaloes, we expect that the spatial correlation on scales of < 10 kpc is negligible after infalling to the center of a parent halo because of the strong tidal force acting on them.

7 RESULT

Firstly, we show the magnification perturbation per a lensed image η in figure 3. The expected contribution $\eta \sim 0.05$ from subhaloes is not sufficient to explain the observed values $\eta \sim 0.10$ especially for lens systems with a high source redshift $z_S > 3$. Although the expected contribution $\eta \sim 0.1$ from line-of-sight structures is sufficient for explaining observed values, the addition of contribution from subhaloes improves the fit especially for systems with a low redshift $z_L < 1.5$ and the overall fit still remains good.

Secondly, we show the strength of convergence perturbation $|\delta\kappa|$ in z_S assuming statistical isotropy for perturbations in figure 4. The observed values (red disks) seem to increase with the source redshift z_S . This is consistent with an interpretation that the dominant contribution comes from the line-of-sight structures (blue diamonds), because the surface density increases with the comoving length to the source. On the other hand, correlation between $\delta\kappa$ from subhaloes and z_S seems to be weak (blue disks). Out of 11 samples, MG0414+0534 shows the largest convergence perturbation $\delta\kappa = 0.0059^{+0.0006}_{-0.0004}$ from subhaloes. Note that the ambiguity in the infall redshift of subhaloes induces errors of just 5 to 10 percent in $\langle |\delta\kappa| \rangle$, which fall within the size of circles in figure 4. However, the observed value $|\delta\kappa_{\text{obs}}| = 0.011 \pm 0.003$ is much larger. For other systems, the convergence perturbation due to subhaloes are much smaller and more difficult to fit to the data. The mean value for the subhaloes is $\langle \delta\kappa_{\text{sub}} \rangle = 0.003$ whereas that for the line-of-sight structures is $\langle |\delta\kappa_{\text{los}}| \rangle = 0.008$ and that for the observed values is $\langle |\delta\kappa_{\text{obs}}| \rangle = 0.009$. Using the mean convergence at the positions of lensed images in the best-fitted model, the mean of the ratio of a projected dark matter mass fraction in subhaloes is just $\langle f_{\text{sub}} \rangle = 0.006$ whereas that for the line-of-sight structures is $\langle f_{\text{los}} \rangle = 0.017$ and that for the observed values is $\langle f_{\text{obs}} \rangle = 0.019$. Thus, it is difficult to explain the observed convergence perturbations by contribution from only subhaloes.

Thirdly, we show the strength of convergence perturbation $|\delta\kappa|$ in z_L assuming statistical isotropy for perturbations in figure 5. It seems that it is consistent with an interpretation that the dominant contribution comes from subhaloes. This may be due to the fact that R_E/R_{200} increases with z_L (figure 6). The reason is as follows. Suppose that the effective Einstein angular radius $\theta_E \sim 1''$ is constant. Then, the effective Einstein radius $R_E = D_L\theta_E$ increases in z_L until $z_L \sim 1.5$ (blue curve in figure 6). Then R_E begin to decrease slowly due to cosmic expansion. For $z_L < 2.0$, however, this effect is small. As we have shown in section 2, the ratio of convergence perturbation of subhaloes $\delta\kappa = \kappa_S$ to the convergence κ_0 of the lensing galaxy halo increases with $R_E = R_{2D}$. Since $\kappa_0 \sim 0.5$ (i.e., the lensed images are near

the critical curve in an SIE), we expect that $\delta\kappa$ increases with R_E hence, z_L until $z_L \sim 1.5$. However, the expected strength is just $|\delta\kappa| \lesssim 0.005$ whereas the observed values are $|\delta\kappa| \lesssim 0.001$. As shown in the upper right panel in figure 5, the contribution from line-of-sight structures have a weak dependence on z_L . This dependence may come from a weak correlation between z_S and z_L . For a given z_S , the possibility of a strong lensing is maximum at z_L where the critical surface density Σ_{crit} , which is inversely proportional to $L = D_LD_S/D_{LS}$, is the lowest. In figure 7, we plotted redshifts z_S, z_L of 11 samples with contours of L , which can be regarded as the PDF of strong lensing. Although the sample is sparse, the histogram of angles $\theta = z_L/z_S$ has its peak at $\theta = 10 - 20^\circ$, which is consistent with the result obtained from L integrated along θ . Thus, it is reasonable to conclude that the weak z_L dependence of $\delta\kappa$ comes from line-of-sight structures as well as subhaloes.

Finally, we show an imprint of asymmetry in the redshift dependence of $|\delta\kappa|$ between z_S and z_L . In order to determine the origin of anomaly in the flux ratios, we separate the data into a low $z_L < 0.6$ and a high $z_L > 0.6$ subsamples and a low $z_S < 2$ and a high $z_S > 2$ subsamples. As one can see in figure 8, a high $z_L > 0.6$ sample shows a strong correlation between z_S and the observed $\delta\kappa$ whereas a high $z_S > 2$ sample shows a weak correlation between z_L and the observed $\delta\kappa$. The other subsamples do not show any sign of correlation. In order to measure the correlation between the redshift and the convergence perturbation, we fit the data with a linear function $|\delta\kappa| = \alpha + \beta z_L(z_S)$, where α is the base function and β is the gradient. As shown in table 2, for subsamples with $z_L > 0.6$, a null hypothesis that $\beta = 0$ (no correlation) can be rejected at a 98 \sim 99 percent confidence level. On the other hand, for subsamples with $z_S > 2$, the null hypothesis ($\beta = 0$) cannot be rejected at a 90 percent confidence level. This asymmetry shows that the contribution from line-of-sight structures is indeed much larger than that from subhaloes. The apparent correlation between observed $|\delta\kappa|$ with z_L is not statistically significant.

8 ANOMALOUS ANOMALY

If the line-of-sight structures are the primary cause of the flux ratio anomaly, we expect a contribution from positive and negative density perturbations almost equally after subtracting the convergence averaged within the effective Einstein radius (Takahashi & Inoue 2014). This is due to the spatial correlation in density fluctuations on scales \lesssim kpc. In the CDM models, the cosmic web structures appear on all the scales that exceed the free-streaming scale. Therefore, any clumps formed on walls and filaments should have spatial correlations between them. Moreover, inter-galactic medium may reside along these structures and enhance the lensing effect by these clumps due to radiative cooling. On the other hand, most of subhaloes at an effective Einstein radius R_E are tidally disrupted. Then, the spatial correlation between subhaloes are expected to be suppressed, leading to reduction in the contribution from negative density perturbations. Thus, if the contribution from subhaloes is large, we expect that lensed images of minimum in the arrival time surface tends to be magnified. However, if the contribution from line-of-sight structures is large, *there is a ~ 50 per-*

Table 1. Quadruple Lens Systems

lens system	z_S	z_L	position	flux	N	b''	$\langle \kappa \rangle$	$\log_{10} k_S (h/\text{Mpc})$	$R_E (\text{kpc})$	$R_{200} (\text{kpc})$	M_{200}	m_{200}^{max}	m_{200}^{min}	reference
B1422+231	3.62	0.34	opt/NIR	radio	3	0.78	0.40	4.8	3.9	320	3.4×10^{12}	1.1×10^8	6.6×10^3	(1) (2)
B0128+437	3.124	1.145	opt/NIR	radio	4	0.24	0.52	4.0	2.1	150	9.2×10^{11}	1.3×10^9	7.1×10^4	(1) (3) (4)
SDP.81	3.042	0.2999	submm	submm	4	1.6	0.50	3.7	7.4	470	1.0×10^{13}	2.8×10^7	4.3×10^5	(13)
MG0414+0534	2.639	0.96	opt/NIR	MIR	4	1.1	0.55	4.9	9.0	350	9.0×10^{12}	1.2×10^9	3.3×10^3	(5) (6) (7)
H1413+117	2.55	1.88(★)	opt/NIR	MIR	4	0.57	0.54	5.5	4.9	270	1.1×10^{13}	6.2×10^9	1.0×10^3	(5) (10)
PG1115+080	1.72	0.31	opt/NIR	MIR	2	1.1	0.52	6.0	5.4	410	7.0×10^{12}	6.0×10^8	1.6×10^2	(5) (11)
Q2237+0305	1.695	0.04	opt/NIR	MIR	4	0.9	0.54	7.1	0.74	370	3.8×10^{12}	4.1×10^8	3.4×10^1	(5) (6)
B1608+656	1.394	0.63	opt/NIR	radio	4	0.91	0.67	3.5	6.4	390	8.6×10^{12}	5.6×10^8	5.8×10^3	(2) (8)
B0712+472	1.339	0.406	opt/NIR	radio	3	0.77	0.50	4.8	4.3	350	4.8×10^{12}	1.5×10^9	7.8×10^3	(1) (5)
B2045+265	1.28	0.8673	opt/NIR	radio	4	0.791	0.39	4.9	8.4	490	2.3×10^{13}	6.1×10^8	9.8×10^3	(1) (9)
RXJ1131-1231	0.658	0.295	opt/NIR	MIR(★★)	3	1.8	0.44	3.9	8.4	640	2.5×10^{13}	1.0×10^9	4.9×10^5	(5) (12)

Note: The unit of mass for M_{200} , m_{200}^{max} and m_{200}^{min} is $h^{-1}M_{\odot}$. (★): The lens redshift z_L is obtained from a best-fit model. (★★): The flux of a line emission [OIII]. References: (1) Koopmans et al. (2003) (2) Sluse et al. (2012) (3) Biggs et al. (2004) (4) Lagattuta et al. (2010) (5) CASTLES data base: <http://www.cfa.harvard.edu/castles> (6) Minezaki et al. (2009) (7) MacLeod et al. (2013) (8) Fassnacht et al. (2002) (9) McKean et al. (2007) (10) MacLeod et al. (2009) (11) Chiba et al. (2005) (12) Sugai et al. (2007) (13) (Inoue et al. 2015a)

Table 2. Linear Model Fit of Subsamples (corresponding to red dotted and red dashed lines in right panels in figure 8)

subsample	α	p - value	β	p - value
$z_S > 2$ (with error)	0.0075 ± 0.0020	0.031	0.0046 ± 0.0052	0.45
$z_S > 2$ (without error)	0.0065 ± 0.0025	0.078	0.0046 ± 0.0023	0.13
$z_L > 0.6$ (with error)	-0.0007 ± 0.0017	0.72	0.0046 ± 0.0009	0.014
$z_L > 0.6$ (without error)	-0.0002 ± 0.0023	0.95	0.0048 ± 0.0010	0.018

cent chance of demagnification in minimum images. If this is the case, the probability of observing such an ‘‘anomalous anomaly’’ increases with the source redshift z_S . In order to estimate the probability, we calculate the ratio of the mean strength of convergence perturbation $\delta\kappa$ from subhaloes to that from the total (subhaloes and line-of-sight structures). The contribution from subhaloes is ~ 40 percent of the total at a source redshift $z_S = 0.7$ and decreases monotonically in z_S to ~ 20 percent at $z_S = 3.6$ (figure 9). Assuming that demagnification of a minimum is always caused by line-of-sight structures with a 50 percent of chance, the probability is ~ 30 percent for $z_S = 0.7$ and ~ 50 percent for $z_S = 3.6$, the possibility of finding such an ‘‘anomalous anomaly’’ is expected to be ~ 30 percent for $z_S = 0.7$ and ~ 40 percent for $z_S = 3.6$. Out of 11 samples, systems with a flux ratio anomaly at more than 3σ level are the B1442+231, MG0414+0534, and SDP.81. The ‘‘anomalous anomaly’’ is found in B image of SDP.81 (Inoue et al. 2015a). Therefore, the probability is ~ 30 percent and hence consistent with the prediction. Although the number of current sample is too small to verify this interpretation, a significant increase in the number of quadruple lenses will lead to discoveries of such new type of anomaly in the near future.

9 CONCLUSION AND DISCUSSION

In this paper, we have explored the origin of the observed flux ratio anomaly in quadruple lensing systems. Firstly, based on a semi-analytical formula, we have shown that the surface mass density of subhaloes are nearly constant at the inner region $R_{2D} < R_{-2}$ of a parent galaxy halo where the light-ray of lensed images pass through. Then we found that the expected contribution from subhaloes is not sufficient to explain the observed anomalies especially for lens systems with a high source redshift $z_S > 3$. Although the expected contribution from line-of-sight structures is already sufficient for explaining observed flux ratios, the addition of contribution from subhaloes improves the fit especially for systems with a low redshift $z_L < 1.5$. Secondly, assuming statistical isotropy in perturbations, the measured convergence perturbation seem to increase with the source redshift z_S as well as the lens redshift z_L . Thirdly, we have shown that the observed correlation between measured convergence perturbations with z_S is statistically significant at a 98-99 percent confidence level where as that with z_L is not statistically significant at 90 percent confidence level. This result supports an idea that the dominant contribution

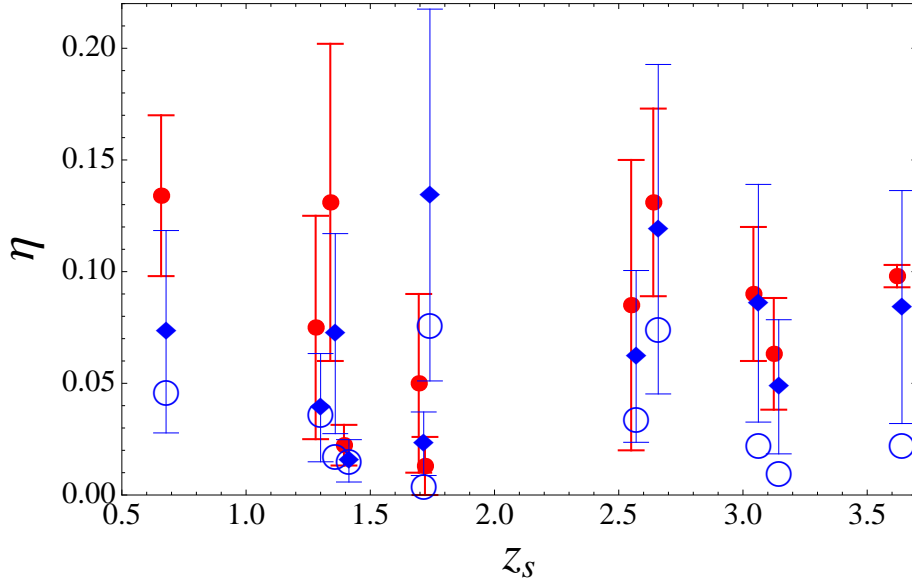


Figure 3. Magnification perturbation η versus the source redshift z_s for 11 quadruple lens samples. Red disks are observed values estimated from the best-fitted models with one-sigma observational error bars. Blue diamonds show the expected contribution from line-of-sight structures with one-sigma error bars. Blue circles show the expected contribution from subhaloes in lensing galaxy haloes. The positions of z_s for the expected values (blue) are slightly shifted for an illustrative purpose.

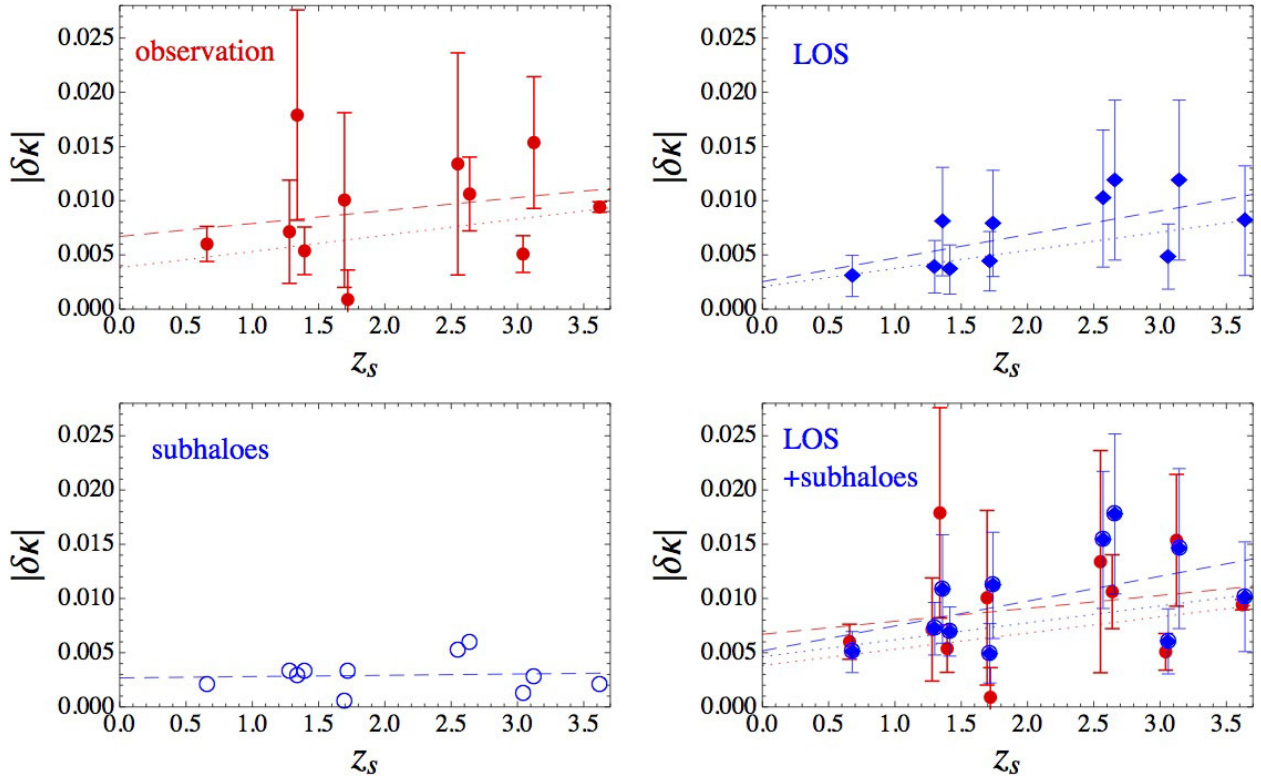


Figure 4. The strength of convergence perturbation $\delta\kappa$ versus the source redshift z_s for 11 quadruple lens samples. The red disks are observed values estimated from the best-fitted models with one-sigma observational error bars. The blue diamonds show the expected contribution from line-of-sight structures with one-sigma theoretical error bars. The blue circles show the expected contribution from subhaloes in a lensing galaxy halo. The errors due to the ambiguity in the infall time of subhaloes are smaller than the size of the blue circles. The blue diamonds embedded in a blue circle show the expected contribution from line-of-sight structures plus subhaloes with one-sigma error bars. Red dotted and red dashed lines correspond to linear model fits to the observed values with and without taking into account the observational errors, respectively. The positions of z_s for the expected values (blue) are slightly shifted for an illustrative purpose.

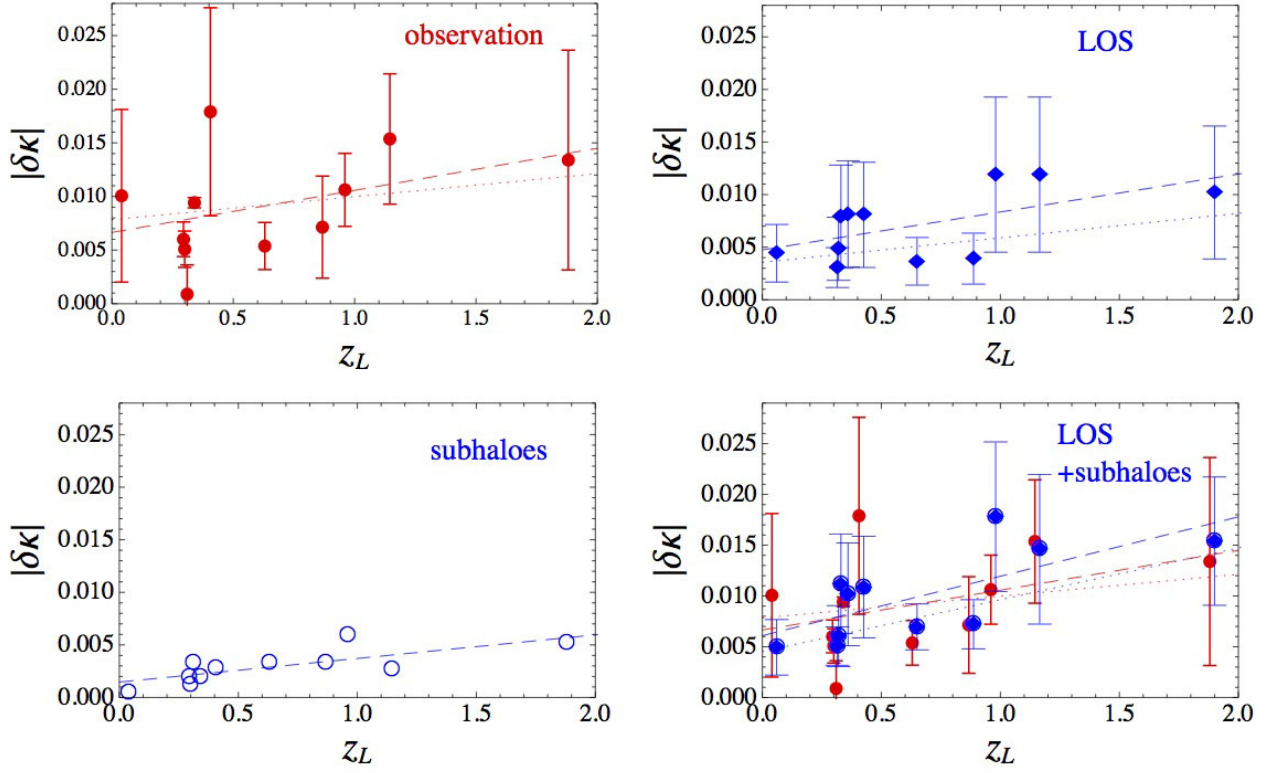


Figure 5. The strength of convergence perturbation $\delta\kappa$ versus the lens redshift z_L for 11 quadruple lens samples. The parameters are the same as in figure 4.

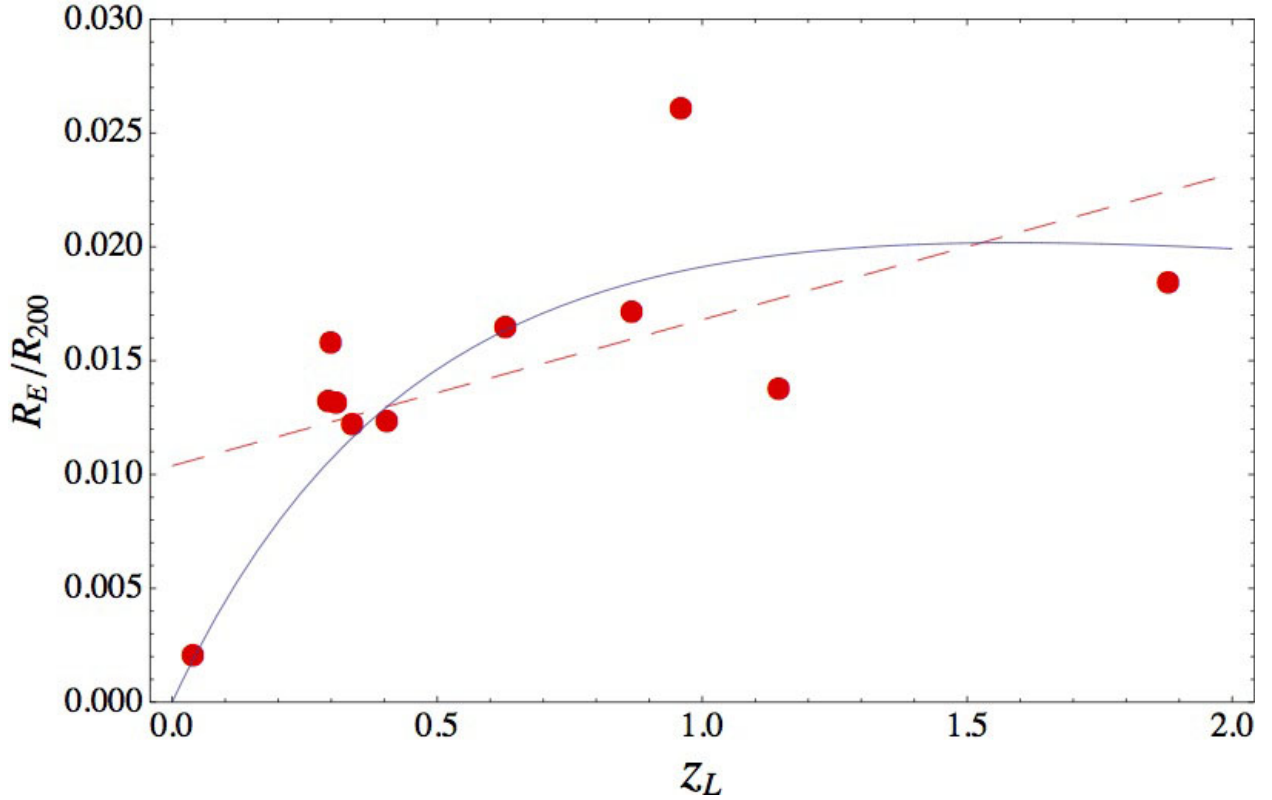


Figure 6. The effective Einstein radius R_E in unit of R_{200} of the lensing galaxies (red disks), the linear model fit (red dashed line), and the angular diameter distance D_L multiplied by a constant that is fitted to the data.

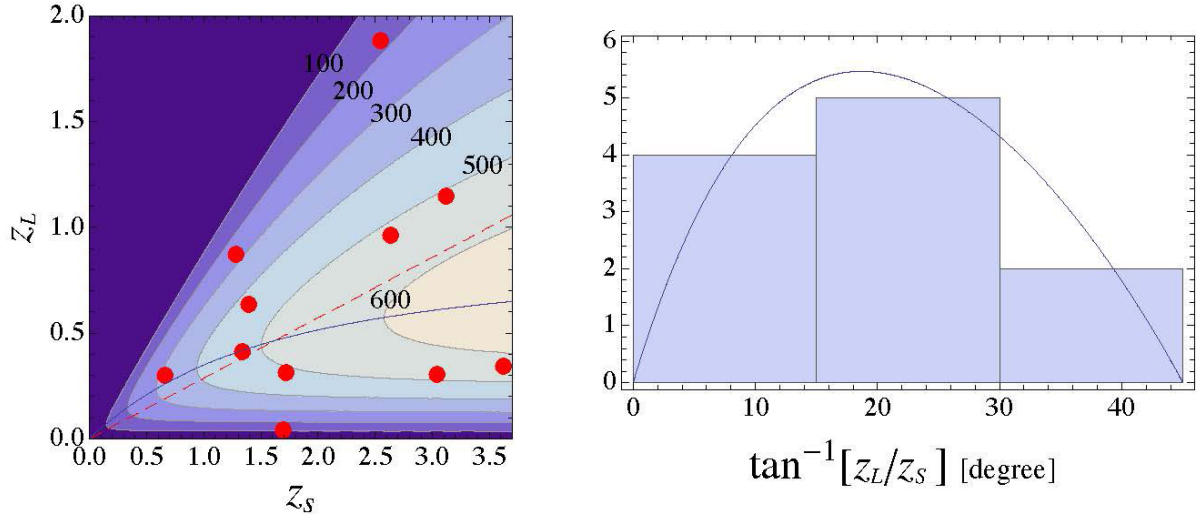


Figure 7. Correlation between the source redshift z_S and the lens redshift z_L . Left: the red disks are observed redshifts for 11 samples and the red dashed line shows a linear model fit without a constant basis. The boundaries of shaded regions represent contours of $L = D_S D_L / D_{LS}$ with a decrement of $100 h^{-1} \text{Mpc}$. The blue curve is the ridge at which L takes its maximum for a given z_S . Right: The histogram of $\tan^{-1}[z_L/z_S]$ of 11 samples and the distribution obtained from L integrated along z_L/z_S for $z_S < 3.6$.

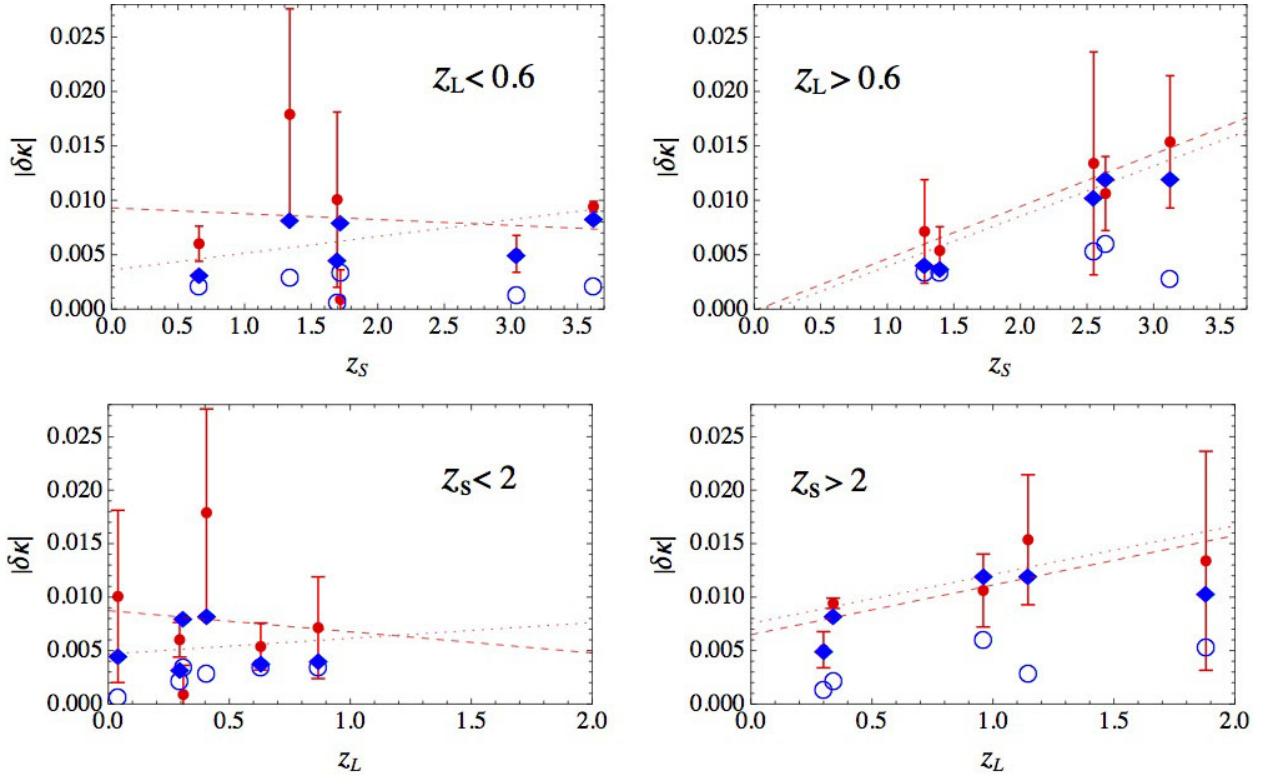


Figure 8. The strength of convergence perturbation $\delta\kappa$ versus the source redshift z_S (upper) and the lens redshift z_L (lower) for 11 samples. The parameters are the same as in figure 4.

comes from line-of-sight structures rather than subhaloes. We have discussed a possible origin of correlations based on a semi-analytic formula. Finally, we have shown that if the contribution from line-of-sight structures is dominant, 30-40 percent of minimum images that show anomaly in the relative flux would be systematically demagnified. The number of systems showing such an ‘‘anomalous anomaly’’ first

found in SDP.81 (Inoue et al. 2015b) would increase with the source redshift z_S .

Our result for substructure lensing is consistent with the previous result, which was obtained using R_{cusp} and R_{fold} (Xu et al. 2015). Out of 11 lenses, MG0414+0534 showed the largest convergence perturbation $\delta\kappa = 0.0059$ from subhaloes but the value is too small to account for the observed

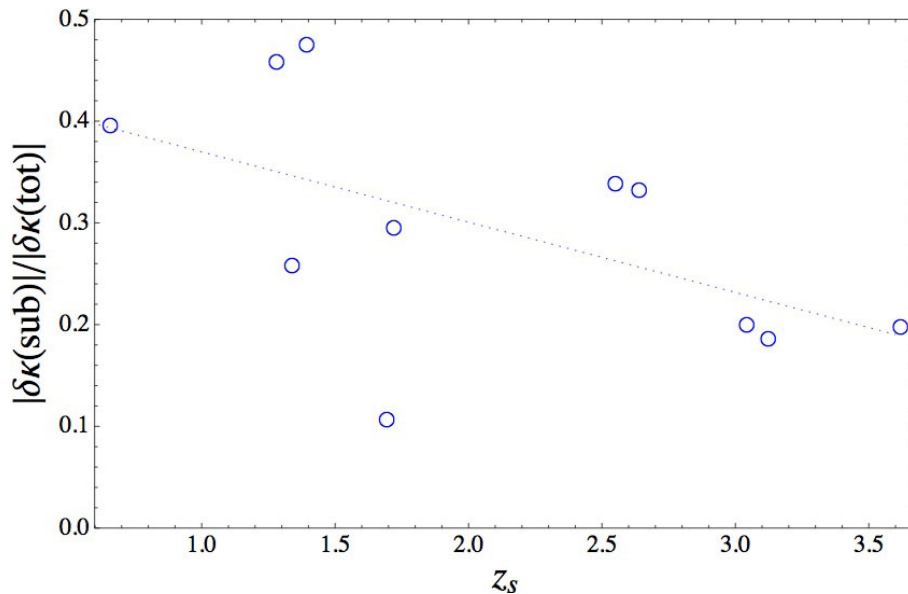


Figure 9. The ratio of the strength of convergence perturbation from subhaloes to that of the total (subhaloes plus line-of-sight structures) shown in blue circles and the linear model fit shown in a blue dotted line.

flux ratios. We have taken into account the astrometric shifts due to subhaloes and use a weak+strong lens decomposition assuming a smooth potential that is similar to an SIS (or SIE) for modeling the unperturbed primary lens. Although our approach suffers from inadequate lens modeling, systematic errors due to the magnification bias and extra lenses do not affect our constraints. Our obtained value for the mean substructure mass fraction $\langle f_{\text{sub}} \rangle = 0.006$ is consistent with the value $f_{\text{sub}} = 0.0064^{+0.0080}_{-0.0042}$ obtained from SLAC lenses for a substructure mass function slope $\alpha = 0.90$ ($\tilde{\alpha} = 1.90$) (Vegetti et al. 2014). Thus, as long as baryonic physics does not significantly affect the result, it is reasonable to conclude that CDM substructures are not the entire reason for the flux anomaly problem.

On the other hand, our result for line-of-sight lensing significantly differs from the result which was obtained using R_{cusp} and R_{fold} (Xu et al. 2012). The difference may come from the typical source redshift $z_s = 2$ assumed in Xu et al. (2012). In fact, our result indicates that for $z_s < 2$, the ratio of the strength of convergence perturbation from subhaloes to that of the total value is 30 to 40 percent. For higher source redshifts, however, the ratio becomes much smaller. Moreover, the two lens systems B2045+265 and B1555+375 used in (Xu et al. 2012) (the latter was excluded in our analysis), which have a relatively large $R_{\text{cusp}} = 0.4 \sim 0.5$ show another source of anomaly: B2045+265 has a secondary lens (McKean et al. 2007) and B1555+375 has a edge-on disk component that can account for the anomaly (Hsueh et al. 2016). Excluding these complex lenses would surely weaken the discrepancy with our result. Complex lens environments such as secondary lenses and disk components and neighbouring groups and clusters should be taken into account properly.

Our result indicates that a secondary lens can reside in the intergalactic space and not necessarily a companion of the primary lens. Furthermore, the previously claimed subhalo with a mass of $(1.9 \pm 0.1) \times 10^8 M_\odot$ discovered from the

residual image of an Einstein ring in B1938+666 (Koopmans 2005; Vegetti et al. 2012) may not be the subhalo of the primary lensing galaxy halo. It can be isolated from any haloes or belonging to another distant one. In order to measure the redshift of a secondary or that of a third lens, we can use the distortion pattern of an extended source and future submillimetre observations would be able to detect such small signals (Inoue & Chiba 2005b,a). With the aid of Atacama Large Millimetre/Submillimetre Array (ALMA), detection of other “anomalous anomaly” in lensed quadruple SMGs will be achieved by increasing the number of anomalous targets to $\gtrsim 10$, which can test our findings.

10 ACKNOWLEDGMENTS

The author thanks Masashi Chiba and Takeo Minezaki for valuable discussion and useful comments. This work is supported in part by JSPS Grant-in-Aid for Scientific Research (B) (No. 25287062) “Probing the origin of primordial minihalos via gravitational lensing phenomena”.

APPENDIX A: UNIQUENESS IN DECOMPOSITION OF STRONG+WEAK LENS

In what follows, we probe uniqueness in decomposition of a strong and weak lens that creates a quadruple image. We assume that the gravitational potential Ψ of a primary lens is sufficiently smooth and similar to that of an SIS and the lens is successfully fitted. We show that reparametrisation of dimensionless model parameters \mathbf{C} and the source angular position \mathbf{y} of the best-fitted model with $\Psi(\mathbf{C})$ does not recover the original fit in the positions if the j -th lensed image at an angular position of \mathbf{x}_j is significantly perturbed to $\mathbf{x}_j + \delta\mathbf{x}_j$, where $|\delta\mathbf{x}_j|$ far exceeds the observational error ε except for a special case in which $\delta\mathbf{x}_j$ is parallel to the tangential arc. For brevity without loss of generality, we set

the effective Einstein radius of the best-fitted model to 1 and all the 1σ errors of observed positions of lensed images to a constant $\varepsilon \ll 1$.

The unperturbed lens equation for the i -th image ($i = 1, 2, 3, 4$) is

$$\mathbf{y} = \mathbf{x}_i - \boldsymbol{\alpha}(\mathbf{x}_i; \mathbf{C}), \quad (\text{A1})$$

where $\boldsymbol{\alpha}(\mathbf{x}_i; \mathbf{C})$ denotes the deflection angle obtained from $\Psi(\mathbf{C})$. Suppose that the j -th lensed image placed at the neighbourhood of a critical curve in the unperturbed lens is affected by a local perturber so that the position of the j -th lensed image is shifted from \mathbf{x}_j to $\mathbf{x}'_j = \mathbf{x}_j + \delta\mathbf{x}_j$ where $|\delta\theta_j| = \eta \gg \varepsilon$ whereas other lensed images at \mathbf{x}_i , ($i \neq j$) remain the observed positions within ε . Then, we need to adjust the position \mathbf{x}'_j back to \mathbf{x}_j by changing the lens parameter \mathbf{C} to $\mathbf{C}' = \mathbf{C} + \delta\mathbf{C}$ and the source position \mathbf{y} to $\mathbf{y}' = \mathbf{y} + \delta\mathbf{y}$ keeping the positions of other lensed images within ε . From the perturbed lens equation and the unperturbed lens equation (A1), we have

$$\delta\mathbf{y} \approx - \left. \frac{\partial \mathbf{y}}{\partial \mathbf{x}} \right|_{\mathbf{x}_j} \delta\mathbf{x}_j - \frac{\partial \boldsymbol{\alpha}_j}{\partial \mathbf{C}} \delta\mathbf{C} \quad (\text{A2})$$

where $\boldsymbol{\alpha}_j = \boldsymbol{\alpha}(\mathbf{x}_j; \mathbf{C})$. Using an orthogonal transformation, the inverse magnification matrix $\partial\mathbf{y}/\partial\mathbf{x}$ can be diagonalized as

$$\frac{\partial \mathbf{y}}{\partial \mathbf{x}} = \begin{pmatrix} 1 - \kappa - \gamma & 0 \\ 0 & 1 - \kappa + \gamma \end{pmatrix}, \quad (\text{A3})$$

where κ and γ are the convergence and shear, respectively. Assuming that the lensed images are significantly magnified and Ψ is similar to that of an SIS, we have $\kappa = \gamma \sim 0.5$. Then, we have

$$\frac{\partial \mathbf{y}}{\partial \mathbf{x}} \sim \begin{pmatrix} 0 & 0 \\ 0 & 1 \end{pmatrix}, \quad (\text{A4})$$

and thus the order of $(\partial\mathbf{y}/\partial\mathbf{x})\delta\mathbf{x}_j$ is η except for the case in which $\delta\mathbf{x}_j \sim (\delta x_j, 0)$, i.e., parallel to the tangential arc. On the other hand, $O[(\partial\mathbf{y}/\partial\mathbf{x})\delta\mathbf{x}_i] = \varepsilon$, ($i \neq j$) or smaller (O denotes order). Since

$$\left. \frac{\partial \mathbf{y}}{\partial \mathbf{x}} \right|_{\mathbf{x}_i} \delta\mathbf{x}_i + \frac{\partial \boldsymbol{\alpha}_i}{\partial \mathbf{C}} \delta\mathbf{C} = \left. \frac{\partial \mathbf{y}}{\partial \mathbf{x}} \right|_{\mathbf{x}_k} \delta\mathbf{x}_k + \frac{\partial \boldsymbol{\alpha}_k}{\partial \mathbf{C}} \delta\mathbf{C}, \quad (\text{A5})$$

for $i \neq j$ and $k \neq j$, and

$$O \left[\left| \frac{\partial \boldsymbol{\alpha}_i}{\partial \mathbf{C}} \delta\mathbf{C} \right| \right] = O \left[\frac{\alpha_i}{C} \delta\mathbf{C} \right] = O \left[\frac{\delta\mathbf{C}}{C} \right], \quad (\text{A6})$$

because of smoothness of Ψ , we have $O[\delta\mathbf{C}/C] \leq \varepsilon$ and $O[|\delta\mathbf{y}|] \leq \varepsilon$. However, equation (A2) and (A4) give $O[|\delta\mathbf{y}|] = \eta$. Thus, we cannot find any reparamerisation except for the case in which $\delta\mathbf{x}_j$ is parallel to the tangential arc. In other words, a massive local perturber that causes a large astrometric shift make the unperturbed model significantly differ from a smooth SIS.

REFERENCES

ALMA Partnership et al., 2015, *ApJ*, **808**, L4
 Barnabè M., Czoske O., Koopmans L. V. E., Treu T., Bolton A. S., 2011, *MNRAS*, **415**, 2215
 Biggs A. D., Browne I. W. A., Jackson N. J., York T., Norbury M. A., McKean J. P., Phillips P. M., 2004, *MNRAS*, **350**, 949

Chen J., Kravtsov A. V., Keeton C. R., 2003, *ApJ*, **592**, 24
 Chen J., Rozo E., Dalal N., Taylor J. E., 2007, *ApJ*, **659**, 52
 Chiba M., 2002, *ApJ*, **565**, 17
 Chiba M., Minezaki T., Kashikawa N., Kataza H., Inoue K. T., 2005, *ApJ*, **627**, 53
 Correa C. A., Wyithe J. S. B., Schaye J., Duffy A. R., 2015, *MNRAS*, **452**, 1217
 Dalal N., Kochanek C. S., 2002, *ApJ*, **572**, 25
 Emberson J. D., Kobayashi T., Alvarez M. A., 2015, *ApJ*, **812**, 9
 Fadely R., Keeton C. R., 2012, *MNRAS*, **419**, 936
 Fassnacht C. D., Xanthopoulos E., Koopmans L. V. E., Rusin D., 2002, *ApJ*, **581**, 823
 Gao L., Navarro J. F., Frenk C. S., Jenkins A., Springel V., White S. D. M., 2012, *MNRAS*, **425**, 2169
 Han J., Cole S., Frenk C. S., Jing Y., 2015, preprint, ([arXiv:1509.02175](https://arxiv.org/abs/1509.02175))
 Hsueh J.-W., Fassnacht C. D., Vegetti S., McKean J. P., Spingola C., Auger M. W., Koopmans L. V. E., Lagattuta D. J., 2016, preprint, ([arXiv:1601.01671](https://arxiv.org/abs/1601.01671))
 Humphrey P. J., Buote D. A., 2010, *MNRAS*, **403**, 2143
 Inoue K. T., Chiba M., 2003, *ApJ*, **591**, L83
 Inoue K. T., Chiba M., 2005a, *ApJ*, **633**, 23
 Inoue K. T., Chiba M., 2005b, *ApJ*, **634**, 77
 Inoue K. T., Takahashi R., 2012, *MNRAS*, **426**, 2978
 Inoue K. T., Minezaki T., Matsushita S., Chiba M., 2015a, preprint, ([arXiv:1510.00150](https://arxiv.org/abs/1510.00150))
 Inoue K. T., Takahashi R., Takahashi T., Ishiyama T., 2015b, *MNRAS*, **448**, 2704
 Keeton C. R., Gaudi B. S., Petters A. O., 2003, *ApJ*, **598**, 138
 Kochanek C. S., Dalal N., 2004, *ApJ*, **610**, 69
 Koopmans L. V. E., 2005, *MNRAS*, **363**, 1136
 Koopmans L. V. E., et al., 2003, *ApJ*, **595**, 712
 Koopmans L. V. E., et al., 2009, *ApJ*, **703**, L51
 Kormann R., Schneider P., Bartelmann M., 1994, *Astronomy and Astrophysics*, **284**, 285
 Lagattuta D. J., Auger M. W., Fassnacht C. D., 2010, *ApJ*, **716**, L185
 MacLeod C. L., Kochanek C. S., Agol E., 2009, *ApJ*, **699**, 1578
 MacLeod C. L., Jones R., Agol E., Kochanek C. S., 2013, *ApJ*, **773**, 35
 Mao S., Schneider P., 1998, *MNRAS*, **295**, 587
 McKean J. P., et al., 2007, *MNRAS*, **378**, 109
 Metcalf R. B., 2005, *ApJ*, **629**, 673
 Metcalf R. B., Madau P., 2001, *ApJ*, **563**, 9
 Metcalf R. B., Moustakas L. A., Bunker A. J., Parry I. R., 2004, *ApJ*, **607**, 43
 Minezaki T., Chiba M., Kashikawa N., Inoue K. T., Kataza H., 2009, *ApJ*, **697**, 610
 More A., McKean J. P., More S., Porcas R. W., Koopmans L. V. E., Garrett M. A., 2009, *MNRAS*, **394**, 174
 Oguri M., Rusu C. E., Falco E. E., 2014, *MNRAS*, **439**, 2494
 Planck Collaboration et al., 2014, *Astronomy and Astrophysics*, **571**, A1
 Sluse D., Chantry V., Magain P., Courbin F., Meylan G., 2012, *Astronomy and Astrophysics*, **538**, A99
 Springel V., et al., 2008, *MNRAS*, **391**, 1685
 Sugai H., Kawai A., Shimono A., Hattori T., Kosugi G., Kashikawa N., Inoue K. T., Chiba M., 2007, *ApJ*, **660**, 1016
 Takahashi R., Inoue K. T., 2014, *MNRAS*, **440**, 870
 Vegetti S., Lagattuta D. J., McKean J. P., Auger M. W., Fassnacht C. D., Koopmans L. V. E., 2012, *Nature*, **481**, 341
 Vegetti S., Koopmans L. V. E., Auger M. W., Treu T., Bolton A. S., 2014, *MNRAS*, **442**, 2017
 Xu D. D., et al., 2009, *MNRAS*, **398**, 1235
 Xu D. D., Mao S., Cooper A. P., Wang J., Gao L., Frenk C. S., Springel V., 2010, *MNRAS*, **408**, 1721
 Xu D. D., Mao S., Cooper A. P., Gao L., Frenk C. S., Angulo R. E., Helly J., 2012, *MNRAS*, **421**, 2553

Xu D., Sluse D., Gao L., Wang J., Frenk C., Mao S., Schneider
P., Springel V., 2015, [MNRAS](#), **447**, 3189